The HKU Scholars Hub   The University of Hong Kong   香港大學學術庫

Title	**Modeling of Soft Fiber-Reinforced Bending Actuators**
Author(s)	**Polygerinos, P; Wang, Z; Overvelde, J; Galloway, K; Wood, R; Bertoldi, K; Walsh, C**
Citation	**IEEE Transactions on Robotics, 2015, v. 31, p. 778-789**
Issued Date	**2015**
URL	**http://hdl.handle.net/10722/211791**
Rights	**Creative Commons: Attribution 3.0 Hong Kong License**

Modeling of Soft Fiber-Reinforced Bending Actuators

Panagiotis Polygerinos, *Member, IEEE*, Zheng Wang, *Member, IEEE*, Johannes T. B. Overvelde, Kevin C. Galloway, Robert J. Wood, Katia Bertoldi, and Conor J. Walsh, *Member, IEEE*

Abstract—**Soft fluidic actuators consisting of elastomeric matrices with embedded flexible materials are of particular interest to the robotics community because they are affordable and can be easily customized to a given application. However, the significant potential of such actuators is currently limited as their design has typically been based on intuition. In this paper, the principle of operation of these actuators is comprehensively analyzed and described through experimentally validated quasi-static analytical and finite-element method models for bending in free space and force generation when in contact with an object. This study provides a set of systematic design rules to help the robotics community create soft actuators by understanding how these vary their outputs as a function of input pressure for a number of geometrical parameters. Additionally, the proposed analytical model is implemented in a controller demonstrating its ability to convert pressure information to bending angle in real time. Such an understanding of soft multimaterial actuators will allow future design concepts to be rapidly iterated and their performance predicted, thus enabling new and innovative applications that produce more complex motions to be explored.**

Index Terms—**Bending, fiber reinforced, fluidic actuator, modeling, soft robot.**

I. INTRODUCTION

SOFT robotics is a rapidly growing research field that combines robotics and materials chemistry, with the ability to preprogram complex motions into flexible elastomeric materials (Young's modulus $\sim 10^2 - 10^6$ Pa) [1]–[4]. These soft systems are engineered using low-cost fabrication techniques, provide adaptable morphology in response to environmental changes, and are ideally suited for gripping and manipulating delicate objects [2]–[7].

Soft actuators are commonly constructed as monolithic structures from compliant materials such as electroactive polymers [8]–[10], shape memory alloys [11], [12], elastomers [2], hydrogels [13], [14], or composites that undergo a solid-state phase transition [15]. Their actuation can be achieved by a variety of stimuli, including electrical charges [9]–[12], chemical reactions [16], [17], and pressurized fluids [2], [3], [7], [15]–[22]. In particular, pneumatic and hydraulic powered soft actuators are promising candidates for robotics applications because of their lightweight, high power-to-weight ratio, low material cost, and ease of fabrication with emerging digital fabrication techniques [15]–[19], [23]. Upon pressurization, embedded chambers in the soft actuator expand in the directions associated with low stiffness and give rise to bending [2], twisting [24], and extending/contracting motions [25]. Furthermore, these actuators can be integrated into the structure of soft robotic systems both as actuators and structural elements [2], [3], [5], [7], [18], [25], [26]. For a more comprehensive view on the soft robotic literature, the authors refer to review works of Majidi [1], Trivedi *et al.* [27], and Kim *et al.* [28].

While empirical approaches have highlighted the exciting potential of soft actuators, the lack of robust models for soft multimaterial fluidic actuators is greatly limiting their potential. Predicting a soft actuator's performance (e.g., deformation and force output in response to a pressurized fluid) prior to manufacture is nontrivial due to the nonlinear response and complex geometry. One class of soft actuators that has received significant research attention in recent years are soft bending actuators, but limited modeling work has been conducted. To make these actuators widely applicable, a systematic understanding of the relationship between actuator geometry and its performance is required.

In this study, soft actuators are considered that are activated by pressurized air and are constructed from a combination of elastomeric (hyperelastic silicones) and inextensible materials (fabrics and fibers), i.e., soft fiber-reinforced bending actuators (see Fig. 1) [8], [29]–[31]. Compared with existing geometrically complex soft bending actuator designs with bellows [2], [3], [18], [24], the widely used soft fiber-reinforced bending actuators have a much simpler tubular geometry that offers ease of manufacture, and where fibers can be arranged along their length to enable nontrivial deformation modes. In addition, a strain-limiting layer added to one side enables bending. To get deeper insight into the response of the system and be able to efficiently design application-specific soft actuators, quasi-static analytical and finite-element method (FEM) models are developed. Compared with previous FEM models, the proposed 3-D models capture the contact interaction information between the
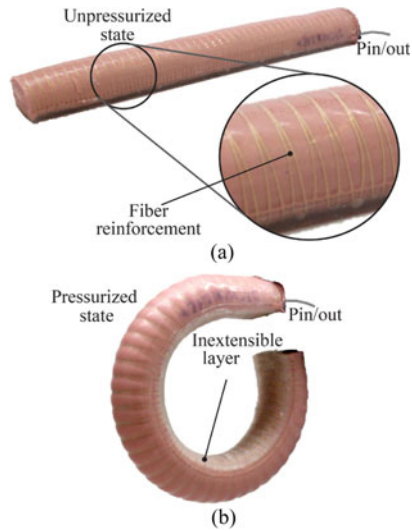
Fig. 1. (a) Soft fiber-reinforced bending actuator in the unpressurized state and a closeup view of the fiber reinforcements (fiber winding). (b) Same actuator in the pressurized state.

straining elastomer material and the nonstraining fiber reinforcements. This enables to capture in a realistic manner the behavior of the bending actuators while providing details about stress concentration points and the generated strains. In addition, a series of experimental tests are conducted to validate the models. In particular, 1) the bending of the actuator in free space and 2) the force applied by the actuator at its proximal tip when in contact with an object are measured. Furthermore, the developed analytical model is used in feedback control loop experiments to demonstrate its ability to perform real-time conversion of the supplied air pressure signal into bending angle information.

II. ACTUATOR FABRICATION

The widely used design of the soft fiber-reinforced bending actuator is in this study fabricated following a new multistep molding process developed by the authors that ensures faster production times and more robust and repeatable actuator outcomes. This fabrication technique is comprised of four parts: 1) a hemicircle elastomeric air chamber (including the caps at the distal and proximal ends); 2) circumferential fiber windings that run along the length of the chamber; 3) an inextensible base layer; and 4) a soft coating material (sheath) that encapsulates the entire system [31]. The circumferential reinforcement provided by the fibers limits radial expansion and promotes linear extension, while the strain limiting layer at the base restricts linear extension on one face of the actuator. Therefore, as the actuator is pressurized, part of it expands while the strain-limited portion restrains any linear expansion along one surface (see Fig. 1), producing a bending motion. More details about the described fabrication method can also be found at the softroboticstoolkit.com website [38] The Soft Robotics Toolkit is a collection of shared resources to support the design, fabrication, modeling, characterization, and control of soft robotic devices.

To offer complete control over every aspect of the assembled actuator including geometry, material properties, and pattern of fiber reinforcements, a multistep molding approach was used. The molds for the actuator were 3-D printed with an Objet Connex 500 printer. The first rubber layer (Elastosil M4601 A/B Wacker Chemie AG, Germany) [see Fig. 2(a)] used a half round steel rod to define the interior hollow portion of the actuator. Woven fiberglass (S2-6522, USComposites, FL, USA) was glued to the flat face to serve as the strain limiting layer [see Fig. 2(b)]. After molding the first rubber layer, fiber reinforcements were added to the surface [see Fig. 2(c)]. A single Kevlar fiber (0.38-mm diameter) was wound in a double helix pattern around the length of the actuator body. Raised features in the mold were transferred to the actuator surface to define the fiber path for consistency of fiber placement. Fiber reinforcements were further secured by placing the entire assembly into another mold to encapsulate the actuator body in a 1.0-mm-thick silicone layer (Ecoflex-0030 silicone, Smooth-on Inc., PA, USA) [see Fig. 2(d)]. The actuator body was then removed from the mold and the half round steel rod [see Fig. 2(e)]. The first open end was capped by placing it into a small cup of uncured silicone. Once this end cured, a vented screw was fed through the 15-mm-thick silicone cap to form the mechanical connection for the pneumatic tubes (see Fig. 2(e), top right). The other open end was capped in a similar manner (see Fig. 2(e), lower right).

III. ACTUATOR MODELING

In rigid-bodied robots, there are well-defined models to characterize the motion of mechanical linkages and the force they can produce. In this study, both detailed FEM models and computationally inexpensive analytical models of a soft fiber-reinforced bending actuator were pursued to analyze the behavior of the actuator and obtain a relationship between the input air pressure and the bending angle, as well as the relationship between the input air and the output force.

A. Analysis of Actuator Cross-Sectional Shapes

The actuator design can be tuned by varying a number of geometrical parameters including the wall thickness of the air chamber, the length of the actuator, the diameter of the hemicircle chamber shape, and the fiber winding pitch and orientation (see Fig. 3). Changing any of these parameters will result in different performance. Furthermore, the shape of the cross section can also significantly affect the response of the system as the magnitude of the area determines the force generated by the pressure acting on it and it will also influence the stress distribution in the elastic material as it resists expansion. In the past, rectangular (RT), circular (FC), and hemicircular (HC) shapes have been used in soft actuator designs without explicitly comparing their efficiencies [8], [29], [32]. In this study, these three cross-sectional shapes were compared to identify the most effective shape for a soft bending actuator based on which requires the least pressure to bend to the same angle while preserving its original cross-sectional shape.
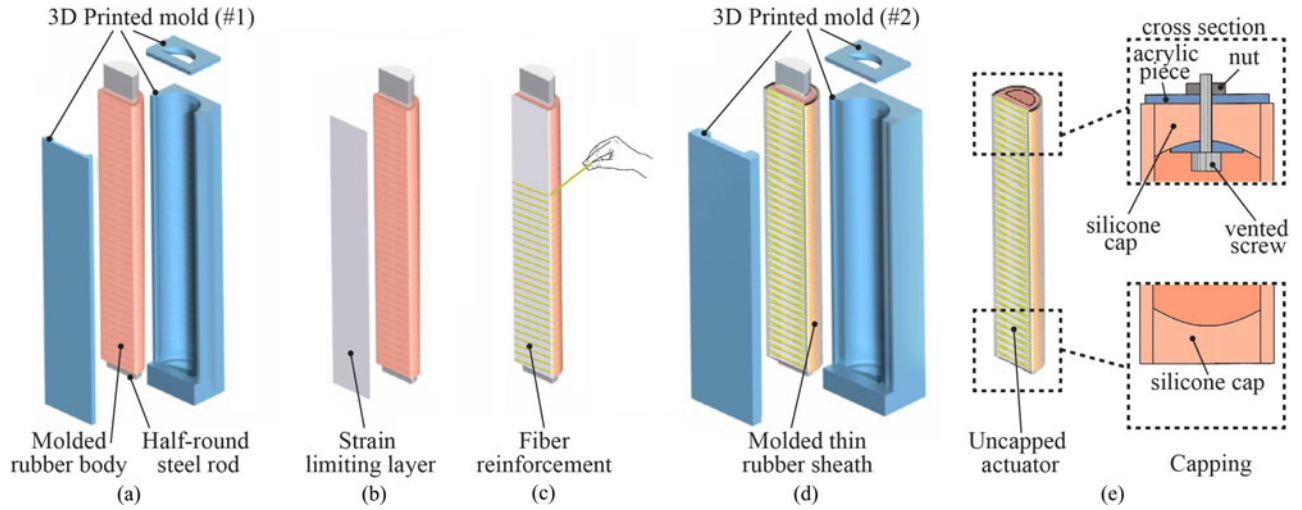
Fig. 2. Schematic outlining some stages of the soft fiber-reinforced bending actuator fabrication process. (a) First molding step using a 3-D printed part. (b) Strain limiting layer (woven fiberglass) is attached to the flat face of the actuator. (c) Thread (Kevlar fiber) is then wound along the entire length of the actuator. (d) Second molding step: the entire actuator is encapsulated in a layer of silicone to anchor all fiber reinforcements. (e) In the final step, the half-round steel rod is removed and both ends of the actuator are capped allowing one end to have a port for the inflow/outflow of air.
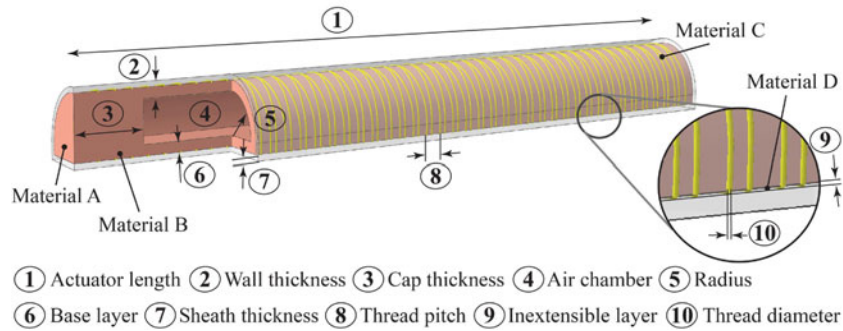

Fig. 3. Soft fiber-reinforced bending actuator showing numbered and labeled the geometrical parameters and design variables that can affect its behavior. Materials A, B, C, and D represent the material properties of the actuator body, sheath, fiber reinforcements, and base inextensible layer, respectively.

The dimensions for each shape were obtained [see Fig. 4(a)] using the same cross-sectional area of a^2, and v is the ratio between rectangular edges. Assuming an actuator wall thickness of $t = a/4$, with an input air pressure of P_{in}, the bending torques (M_a) of internal air pressure against the distal cap of the actuator geometry were calculated as

$$M_a^{RT} = \frac{0.5}{v}a^3 P_{in} \tag{1}$$

$$M_a^{HC} = 0.34a^3 P_{in} \tag{2}$$

$$M_a^{FC} = 0.72a^3 P_{in}. \tag{3}$$

A larger M_a value indicated that a particular shape could generate a larger bending torque for the same input pressure.

To create actuator bending, the torque M_a must overcome the internal bending moments, which are also functions of the actuator geometry. To quantify and compare this effect, the ratio of the actuator internal bending moment and the pressure-generated bending torque M_a is denoted as the bending resistance, and the bending resistance for all three cross-sectional shapes is shown

in Fig. 4(b) for a bending angle ranged from 0° to 360°. A lower vertical axis value indicates an actuator that is theoretically easier to bend, and therefore, the RT shape was found less suitable since it required the highest amount of pressure to reach the same bending angle. On the other hand, the HC was found easier to bend. Additionally, the RT shape was assumed with a ratio (v) of 1.47, such that it could generate a bending torque M_a equal to that of the HC shape when the same amount of pressure P_{in} was provided. As a result, both the RT and FC shapes demonstrated similar bending resistance. Based on the above, the HC shape was chosen for this study.

B. Analytical Modeling

An analytical model was developed that captures the explicit relationship between input pressure, bending angle, and output force by taking into consideration both the hyperelastic material property of silicone rubber and the geometry of the actuator. The variables in the model were actual actuator dimensions and material properties that could be either measured or obtained from calibrations.
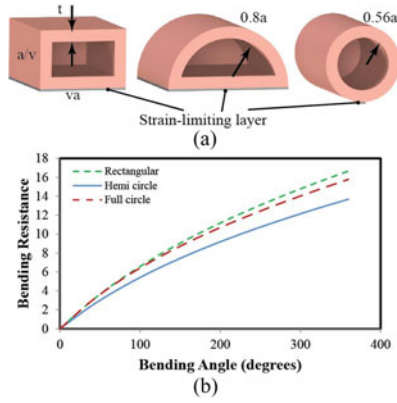
Fig. 4. (a) Cross-sectional views of a rectangular (RT), hemicircle (HC), and full circle (FC) actuator shape with equal cross-sectional area and with a strain limiting layer attached at their bottom face. (b) Efficiency comparison (bending resistance) of the different actuator shapes. A lower bending resistance indicates that an actuator is easier to bend with less pressure.
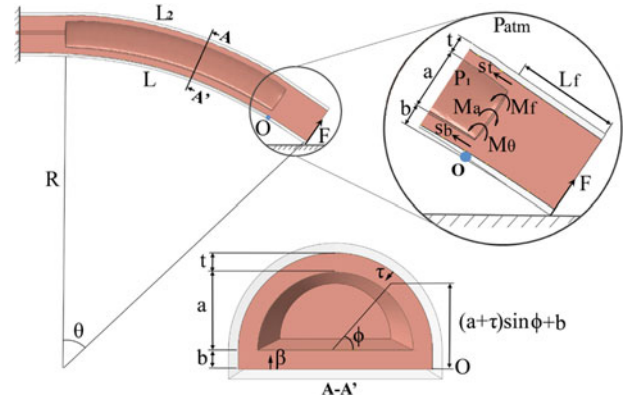

Fig. 5. (Top left) Side view of the soft fiber-reinforced bending actuator in a bending state. Closeup view: view of the actuator distal tip showing the generated moments. Lower center: Cross-sectional view of the actuator.

1) Material Model: The soft fiber-reinforced bending actuators were fabricated using silicone rubber. This was modeled as an incompressible Neo–Hookean (NH) material [33] so that the strain energy is given by

$$W = \frac{\mu}{2} (I_1 - 3) \tag{4}$$

where I_1 is the first invariant of the three (axial, circumferential and radial) principal stretch ratios $\lambda_1, \lambda_2,$ and λ_3 as

$$I_1 = \lambda_1^2 + \lambda_2^2 + \lambda_3^2 \tag{5}$$

and μ is the initial shear modulus of the material. The principal nominal stresses s_i could then be obtained as a function of W, λ_i, and the Lagrange multiplier p as

$$s_i = \frac{\partial W}{\partial \lambda_i} - \frac{p}{\lambda_i}. \tag{6}$$

2) Model for Bending Angle in Free Space: A geometrical model of the soft fiber-reinforced bending actuator that relates the input air pressure and the bending angle in free space is derived fully accounting for large deformations. It was assumed that when compressed air ($P_1 > P_{atm}$) is supplied to the air chamber, the top wall will extend while the bottom layer will be constrained by the inextensible layer, thus causing the actuator to bend toward the bottom layer with a radius R and angle θ (see Fig. 5). Here, the fiber-reinforced mechanism was considered to be a hard constraint to the actuator. Although the actuator has a multilayered structure, for the sake of simplicity, it was modeled as a homogeneous incompressible NH material [33] with effective initial shear modulus $\bar{\mu}$. The dynamics associated with pressurization were neglected in the model, and it was assumed that the actuator always has a uniform bending curvature.

Here, the principal stretch λ_1 along the axial direction of the actuator was denoted. Furthermore, due to the fiber reinforcement constraint, the strain in the circumferential direction was negligible so that $\lambda_2 = 1$. Finally, considering the incompressibility of the material, $\lambda_1 \lambda_2 \lambda_3 = 1$, it was obtained

that

$$\lambda_1 = \lambda, \ \lambda_2 = 1, \ \lambda_3 = \frac{1}{\lambda}. \tag{7}$$

Next, a vanishing stress was assumed in radial direction through the thickness of the actuator (i.e., $s_3 = 0$), and by combining (6) with (4) and (5) as

$$s_1 = \frac{\partial W}{\partial \lambda_1} - \frac{P}{\lambda_1} = \bar{\mu} \left(\lambda - \frac{1}{\lambda^3} \right) \tag{8}$$

$$s_2 = \frac{\partial W}{\partial \lambda_2} - \frac{P}{\lambda_2} = \bar{\mu} \left(1 - \frac{1}{\lambda^2} \right) \tag{9}$$

$$s_3 = \bar{\mu} \lambda_3 - \frac{P}{\lambda_3} = 0 \tag{10}$$

$$p = \bar{\mu} \lambda_3^2 = \frac{\bar{\mu}}{\lambda^2}. \tag{11}$$

Within the range of stretches considered in this application ($1 \leq \lambda < 1.5$), the circumferential stress s_2 was significantly smaller than s_1 (i.e., $s_2 < s_1/2$). Therefore, s_1 was considered to be the only nonvanishing principal stress and hereafter denoted as s.

The internal stretch of the actuator materials resulted in an opposing bending moment. Therefore, at each bending configuration, a torque equilibrium was reached around the fulcrum O, as it is shown in Fig. 5, that can be obtained from

$$M_a = M_\theta \tag{12}$$

where M_a is the bending torque of internal air pressure against the distal cap of the actuator, and M_θ is the combined moment of the stresses s_t and s_b on the top and bottom layers. Using the hemicircular geometry with radius a the distal actuator cap was a, M_a can be calculated as

$$M_a = 2 (P_1 - P_{atm}) \int_0^{\frac{\pi}{2}} (a \sin \vartheta + b) a^2 \cos^2 \vartheta \, d\vartheta$$

$$= \frac{4a^3 + 3\pi a^2 b}{6} (P_1 - P_{atm}). \tag{13}$$

Moreover, combining the effect of the stresses acting on the top and bottom layers, the bending moment is

$$
M_\theta = \int_0^b s_\beta \cdot 2\,(a+t)\,L\beta d\beta
$$
$$
+ 2\int_0^t \left(\int_0^{\frac{\pi}{2}} s_{\tau,\phi} \left((a+\tau)^2 \sin\phi + b\,(a+\tau) \right) L d\phi \right) d\tau. \tag{14}
$$

Furthermore, by introducing the local coordinate β, the longitudinal stretch and strain in the bottom layer can be calculated as (see Fig. 5)

$$
\lambda_\beta = \frac{R+\beta}{R} = \frac{L/\theta + \beta}{L/\theta} = \frac{\beta\theta}{L} + 1 \tag{15}
$$

$$
s_\beta = \bar{\mu}\left(\lambda_\beta - \frac{1}{\lambda_\beta^3} \right). \tag{16}
$$

Similarly, for the top layer with the coordinate τ (see Fig. 5):

$$
\lambda_{\tau,\phi} = \frac{R + b + \sin\phi\,(a+\tau)}{R} \tag{17}
$$

$$
s_{\tau,\phi} = \bar{\mu}\left(\lambda_{\tau,\phi} - \frac{1}{\lambda_{\tau,\phi}^3} \right). \tag{18}
$$

By substitution of (13) and (14) into (12), a relationship between the input air pressure P_{in} and the bending angle θ in free space can be obtained

$$
P_{in} = \frac{6M_\theta\,(\theta)}{4a^3 + 3\pi a^2 b} \tag{19}
$$

where $P_{in} = P_1 - P_{atm}$, a and b are the air chamber radius and bottom thickness of the actuator, respectively, and $M_\theta\,(\theta)$ was given in (14). Substituting (15)–(18) into (14) to eliminate s and λ, it is possible to show that M_θ is a function of $\bar{\mu}, a, b, t,$ and θ. However, the integral in (14) could not be computed analytically, and therefore (14), and hence (19), had to be solved numerically. The material property coefficient $\bar{\mu}$ can be obtained through calibration tests.

3) Model for Bending Torque/Force: An expression for the actuator force can be derived by extending the analytical model previously developed for bending angle. In this analysis, the actuator was assumed to be constrained at a zero bending angle (i.e., constrained in a flat configuration) such that no internal bending moments (M_θ) were generated under pressurization. Therefore, the torque equilibrium at the fulcrum O of Fig. 5 becomes

$$
M_f = FL_f = M_a = \kappa P_{in} \tag{20}
$$

where F is the contact force between the actuator distal cap and the environment, L_f is the distal cap length, M_f is the external bending torque generated by the contact force around O, combining (20) with (13), and κ is a function of the actuator geometry given by

$$
\kappa = \frac{4a^3 + 3\pi a^2 b}{6}. \tag{21}
$$

This equation describes the pressure–force relationship under an isometric process (constant bending angle). Although (20) is only applicable for a specific bending angle (i.e., zero degrees), it does provide insight into the relationship between actuator geometry and bending force. It also follows that under isotonic conditions (constant pressure), the force output will decrease as bending angle increases, because larger bending moments are required to bend the actuator to the desired angle. Hence, the bending force described in (20) can be defined as the maximum force output for a particular input pressure.

C. Finite-Element Method Modeling

The analytical model quickly generates insights into the response of an actuator to pressurized air for a particular geometry. However, it cannot capture certain aspects of the soft actuator behavior such as the interaction of internal layers of different materials. FEM models, on the other hand, provide a more realistic description of the nonlinear response of the system, although at a higher computational cost. An additional advantage of FEM is that the deformation (and stress) in soft actuators can be readily visualized, leading to a better understanding of the influence of local strain on global actuator performance. Prior work on FEM modeling soft elastomeric actuators with fiber reinforcements has demonstrated the shape due to bending [7], [34], but minimal work has been done to validate these models experimentally or used to characterize the actuator stiffness and force-generating capabilities [35], [36].

Prior to simulations, elastomeric samples of the individual materials used to fabricate the actuator were tested according to ASTM D638 (Type IV) at a rate of 500 mm/min for uniaxial tensile strength, and compression samples were compressed at a rate of 500 mm/min to obtain accurate material properties. A hyperelastic incompressible Yeoh material model [37], with strain energy $U = \sum_{i=1}^2 C_i (I_i - 3)$, was used to capture the nonlinear material behavior of both the Elastosil and the Ecoflex materials. In particular, the material coefficients were $C_1 = 0.11 \text{MPa}, C_2 = 0.02 \text{MPa}$ for the Elastosil and $C_1 = 0.012662 \text{MPa}$ and $C_2 = 0 \text{MPa}$ for the Ecoflex. It is noted that the initial shear modulus was $\bar{\mu} = 2C_1$.

To model the behavior of the actuators, 3-D FEM models were constructed and analyzed with ABAQUS/Standard (Simulia, Dassault Systemes). Simplifications in the model were kept to a minimum in order to closely match the experimental setup. The inlet for pressurized air was not taken into account in the model as the pressure was applied to all the internal walls of the chamber. All the components of the actuator were modeled using solid tetrahedral quadratic hybrid elements (Abaqus element type C3D10H). For the thin fiber windings, quadratic beam elements were used (Abaqus element type B32), which were connected to the Elastosil by tie constraints. The material of the fiber winding was modeled as linear elastic (Young's modulus of $E = 31,076 \text{MPa}$ and a Poisson's ratio of $v = 0.36$). The number of nodes and elements used in the models are summarized in Table I.

As expected, the modeled beam elements introduced some bending support, while the fiber windings provided no bending

TABLE I
NUMBER OF NODES AND ELEMENTS FOR THE SOFT ACTUATOR FEM MODELS

Radius (mm)	Length (mm)	Wall Thickness (mm)	Number of Nodes	Number of Elements (B32, C3D10H)
6.0	100	2.0	71 309	44 465
6.0	130	2.0	95 061	59 108
6.0	160	2.0	118 708	73 614
8.0	100	2.0	98 113	62 301
8.0	130	2.0	128 787	81 219
8.0	160	1.0	90 449	55 141
8.0	160	2.0	160 711	101 097
8.0	160	3.0	185 274	118 557
10.0	160	2.0	192 650	121 106
12.0	160	2.0	208 921	131 646

stiffness. To decrease the modeled stiffness from the beam elements, the radius of the beam elements was reduced by a factor of 2. This radius reduction resulted in an insignificant change in tensile strength of the wire as it remained significantly stiffer than the elastomer. It is also noted that although the physical fiber windings did not have any compressive stiffness, the beam elements of the FEM model added some. However, the influence of this effect on the simulation result can be neglected, since all the beams were under tension. Furthermore, for sake of computational efficiency and to increase the convergence of the simulation, the bottom layer of the actuator, consisting of an inextensible layer, was modeled as an elastomer (Yeoh material with $C_{\text{combined}} = 7.9\text{MPa}$). The stiffness of the combined layer remained sufficient to function as an inextensible layer. Finally, to model loading of the actuator, an internal pressure was applied to the surface of the chamber. The deformation of the actuator obtained with the proposed FEM model is illustrated in Fig. 6. Similarly, the previously developed FEM model was also used to conduct a force analysis. In this force model, the proximal cap was completely fixed, and the bending deformation of the actuator was also constrained. The force was then determined by summing the reaction forces at the nodes on the edge of the distal cap.

IV. TESTING OF SOFT FIBER-REINFORCED BENDING ACTUATORS

A. Experimental Platform

An experimental platform was developed (see Fig. 7) to validate the analytical and FEM models. This platform permitted fast and easy characterization and incorporated multiple sensing modalities [31], [36]. Within the platform, the soft actuator proximal cap with the air inlet was clamped in a rigid fixture, emulating the boundary constraints defined with the modeling approaches. The distal cap of the actuator was free to bend in the vertical plane. It is noted that a horizontal bending would be less favorable since gravitational forces could bring the actuator out of plane. A high-definition camera (DSLR, Rebel T2i, Canon Inc., NY, USA), was used to monitor the actuator from the side so that the bending trajectory of its distal cap (tip) could be recorded. The camera was aligned with a checkered background. This technique allowed lens distortion issues to be
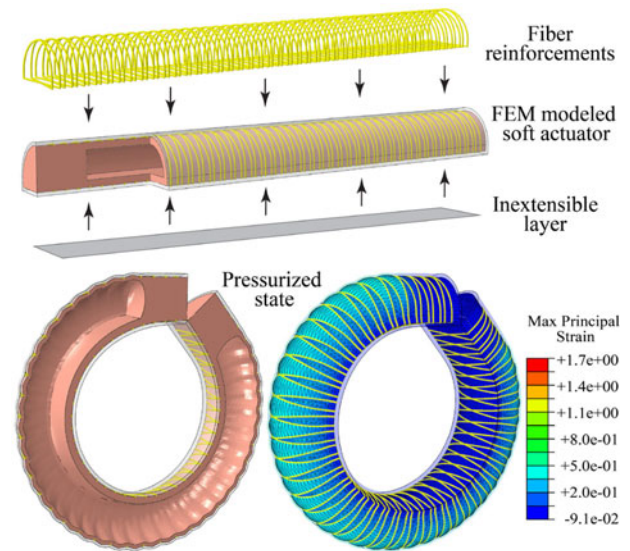

Fig. 6. Three-dimensional FEM model result for the actuator at unpressurized and pressurized state at 196 kPa. (Top) FEM modeled fiber reinforcements, inextensible layer in an unpressurized state. The arrows indicate their location at the soft actuator. (Lower left) The bending angle shape at 360° of the FEM modeled soft actuator in a cross-sectional view demonstrating the air chamber and the fiber reinforcements. (Lower right) Bending angle shape at 360° of the FEM modeled soft actuator in a strain contour view that highlights the maximum principal strain locations and fiber reinforcements.
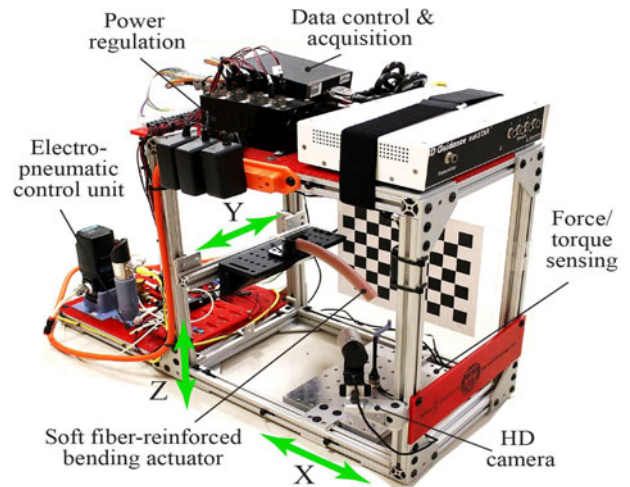
Fig. 7. Evaluation platform with all the associated equipment for monitoring and control of the soft actuator. The evaluation platform is described in [31], [36].

addressed and measurement accuracy to be enhanced. A metric ruler was also placed on the rigid fixture, next to the actuator, to provide a correlation between number of pixels in the picture frames and the actual length. Postprocessing of the video frames was performed with freely available software (Kinovea 0.8.15), where the x and y coordinates of the actuator tip trajectory were tracked and bending angle was calculated. A six-axis force/torque sensor (Nano17, ATI Industrial Automation, NC, USA) was used to measure the force generating capability. A short post was mounted on the force sensor and brought in contact with the tip of the actuator. The actuator top surface was placed in contact with a rigid fixture to minimize nonlinear

effects due to bending. The pressure inside the actuator was gradually increased, while the force exerted by the actuator's tip was recorded. The experiments for each version of the soft fiber-reinforced bending actuators were performed three times to assess accuracy and repeatability.

B. Calibration Process

Five trials were conducted, and a one-step least-squares estimation procedure of $\bar{\mu}$, was obtained using experimentally measured input pressure and bending angles. In each trial, the same actuator was pressurized to bend in free space. Although the estimated $\bar{\mu}$ value was expected to be actuator specific, in reality, the difference was not significant among different actuator samples. The estimated $\bar{\mu}$ value was 0.314 MPa for an actuator with $(a, b, t, L) = (8, 2, 2, 160)$ mm. The same $\bar{\mu}$ value was used in all subsequent studies with good results.

V. VALIDATION AND EXPERIMENTAL RESULTS

A. Evaluation of Analytical and Finite-Element Method Model

To demonstrate the value of the proposed analytical and FEM models, several physical parameters of the actuator (i.e., length, radius, and wall thickness) were varied to evaluate their influence on bending angle at 90°, 180°, and 360° (i.e., full circle) (see Fig. 8). A baseline set of geometrical parameters (160.0-mm length, 2.0-mm wall thickness, and 8.0-mm radius) was chosen as a starting point for the soft actuator where the maximum bending angle (i.e., 360°) could be reached at around 200 kPa (∼30 PSI). These dimensions were chosen as such an actuator would be suitable for wearable robotic applications [35]. An additional six variations of this parameter set were used (e.g., the actuator length was varied while diameter and wall thickness kept constant) to demonstrate the influence of actuator geometry, as presented in Fig. 8. The results from this evaluation presented some deviations in the absolute pressure values. This was mainly due to the assumption in the analytical model that the bottom layer of the actuator remained flat during pressurization. In contrast, this radial bulging was captured by the FEM models resulting in the actuator cases of radius and wall thickness, which were cross section dependent, to deviate more. Nonetheless, both models were found to provide similar trends for all parameter variations. Specifically, the results of Fig. 8(b) showed that for an increase in the length, higher air pressure was required to achieve full 360° bending. Similarly, a decrease in radius required higher air pressures for actuation [see Fig. 8(a)]. Finally, it was shown that as the wall thickness increased, air pressure also had to increase to achieve a given bending angle [see Fig. 8(c)].

B. Bending Angle Experiments

The bending trajectories of the baseline actuator compared with the analytical and the FEM models are illustrated in Fig. 9. A good match between the theoretical and experimental data can be observed from the plot (maximum displacement error of 3.7%), demonstrating the validity and accuracy of the models. In addition, the pressure locations are shown for 0° and 360° bending in Fig. 9. These pressure angle-related locations presented
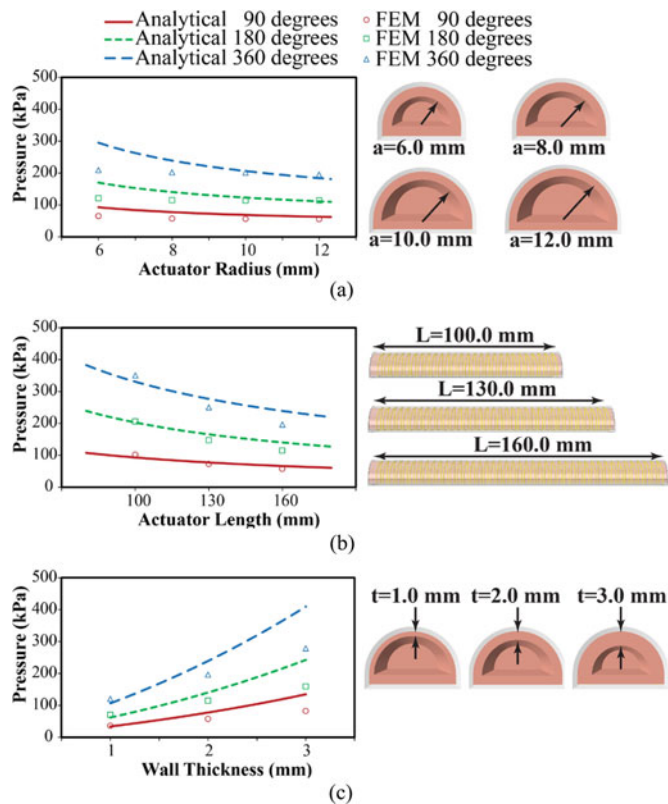

Fig. 8. Analytical and FEM modeling results for the soft fiber-reinforced bending actuator in free space at: 90°, 180°, and 360°. (a) Pressure versus actuator radius, for radius analytical values ranging from 6.0 to 12.0 mm and FEM specific values of 6.0, 8.0, 10.0, and 12.0 mm. (b) Pressure versus actuator length, for analytical length values ranging from 80.0 to 180.0 mm and FEM specific values of 100.0, 130.0, and 160.0 mm. (c) Pressure versus wall thickness, for analytical wall thickness ranging from 1.0 to 3.0 mm and FEM specific values of 1.0, 2.0, and 3.0 mm.

only small discrepancies in pressure values due to some initial prebending (i.e., at 0 kPa) and gravitational influences in the fabricated actuator with a maximum pressure error of 10.9%.

Experimental data were collected with the six variations of actuator designs as described in the previous section. Each actuator was pressurized five times in order to bend in free space, and the supplied pressure along with the corresponding bending angle was measured using the experimental setup of Section IV-A. The contractions occurred at a slow pressure rate of 0.2 Hz in order to avoid any dynamic oscillations. Rates slow as these can still be considered sufficient in some robotic applications where speed of actuation is not of paramount importance. Examples can be in soft rehabilitation devices where range of motion is more important than speed [36]. The averaged measured pressures were used with the analytical and FEM models to calculate actuator bending angles. In Fig. 10, these results are compared with the measured angles from the experiments. The findings demonstrate that both models capture the overall trend of the actuators. The discrepancies showed by the analytical model were potentially a product of linearization of the NH model at large deformations, radial bulging effects at the base layer, and expansion of the elastomer. This nonlinear effect was more apparent in shorter actuators due to the increased pressure, making the bulging more profound. Finally, the experimental results
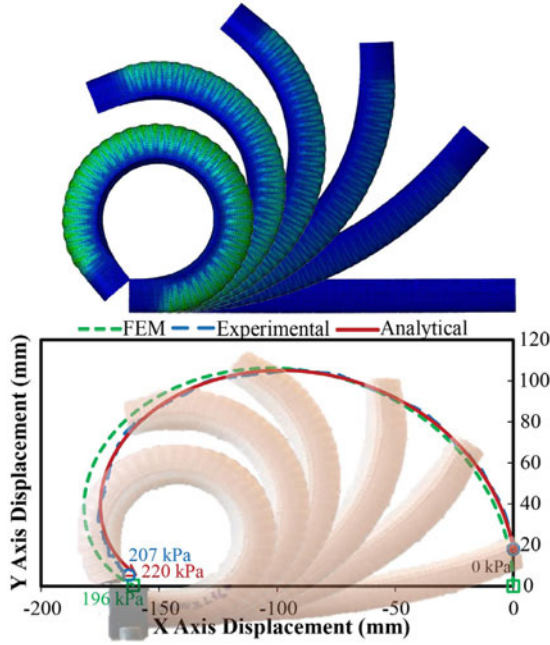
Fig. 9. Soft fiber-reinforced bending actuator tip trajectory for bending angle from 0° to 360°. The experimental results are presented along with the analytical and FEM model predictions. Images of the FEM modeled and physical actuator at different bending angles are overlaid and superimposed with the graph, respectively. The 0.0 kPa and maximum pressure locations are also shown for FEM, experimental, and analytical results.

presented a repeatable nonlinear pattern (s-type curves, Fig. 10). This was possibly due to gravitational forces that acted on the actuators (i.e., in all stages of their bending, the center of gravity of the actuators was changing compared with the path followed by the actuator distal end).

C. Force Experiments

Soft actuators are capable of exerting forces either at their tip or at the interaction points along their body as they conform around an object. As shown in Fig. 11(a), the top layer of the actuator was constrained to minimize nonlinear effects (i.e., the tendency of the actuator to bend when pressurized) and to concentrate the force at the distal cap. This way, the maximum force that could be generated by the actuator at its tip was measured when the distal cap was brought in contact with the force/torque sensor. The experimental results obtained from examining three actuators (two with same radius of 8.0 mm but different lengths of 160.0 and 130.0 to assess the influence of length on force, and one with 6.0-mm diameter and 160.0-mm length to assess influence of radius on force) were compared with the corresponding analytical and FEM models. The results (see Fig. 11) demonstrated the ability of both models in predicting force exertion from the tip of the actuator for this configuration. In particular, the analytical model demonstrated a maximum force error of 4.3% and the FEM model 10.3%. In addition, it was shown that the actuator length has small influence on force generation, whereas changes in radius have a more significant role. In particular, because the κ coefficient of (21) is a function of the actuator radius (a), a decrease in radius leads to significant loss of ability to deliver high forces.
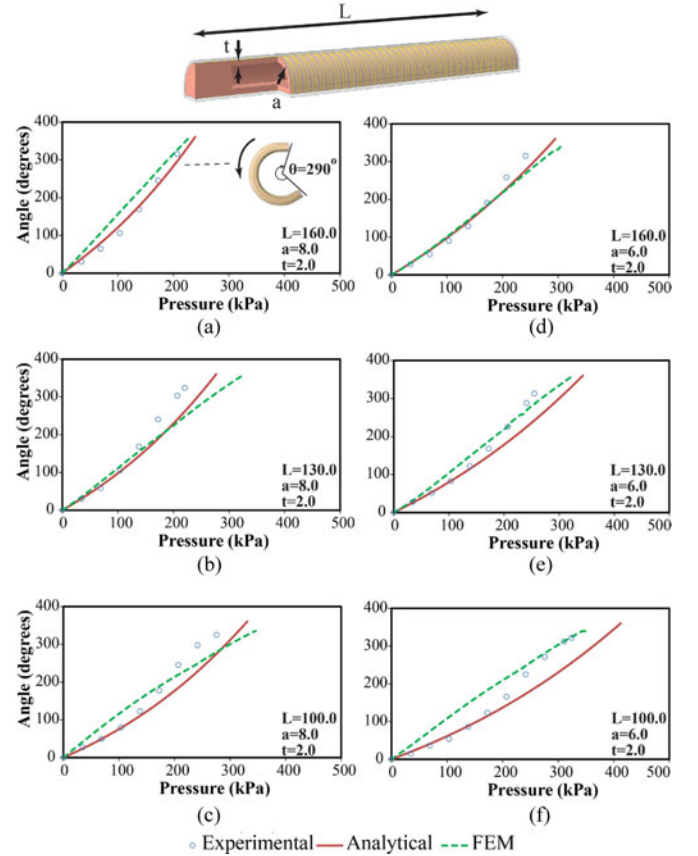

Fig. 10. Input actuator pressure against bending angle results that were obtained from the analytical model, FEM model and experimental data for a bending angle ranging from 0° to 360°. (a) Soft fiber-reinforced bending actuator length 160.0 mm, (b) 130.0 mm, and (c) 100.0 mm, with radius of 8.0 mm and wall thickness of 2.0 mm. (d) Soft fiber-reinforced bending actuator length 160.0 mm, (e) 130.0 mm, and (f) 100.0 mm, with radius of 6.0 mm and wall thickness of 2.0 mm.

VI. SOFT FIBER-REINFORCED BENDING ACTUATOR CONTROL

A feedback control loop with an angle filter, as shown in Fig. 12, was implemented to demonstrate the ability of the analytical model of (19) to use pressure information to estimate bending angle in real time. The control loop was built using the experimental platform of Section IV-A, with a pressure regulator, two pneumatic valves—inlet/outlet (X-valves, Parker Hannifin Corp., OH, USA)—and a pressure sensor (BSP001, Balluff Inc., KY, USA). The two valves were connected to the soft actuator where the inlet was in line with the pressure regulator and the outlet with the air exhaust. Between the two valves, the air pressure P_a of the actuator was measured. Utilizing (19) and the measured input air pressure information P_a, the angle filter of the feedback loop was able to estimate the actuator bending angle θ_a. According to the error angle signal θ_e (i.e., desired angle signal θ_d minus the bending angle θ_a of the actuator), the valve controller C_v with a sampling rate of 100 Hz was used to drive the valves. In particular, positive angle θ_e values indicated that the soft actuator was not bent enough and thus enabled the valve controller to open the inlet and close the outlet valve, and *vice versa*. A deadzone was also introduced at the valve controller to reduce undesired frequent switching of the valves. The deadzone created boundaries around the angle signal θ_e that allowed
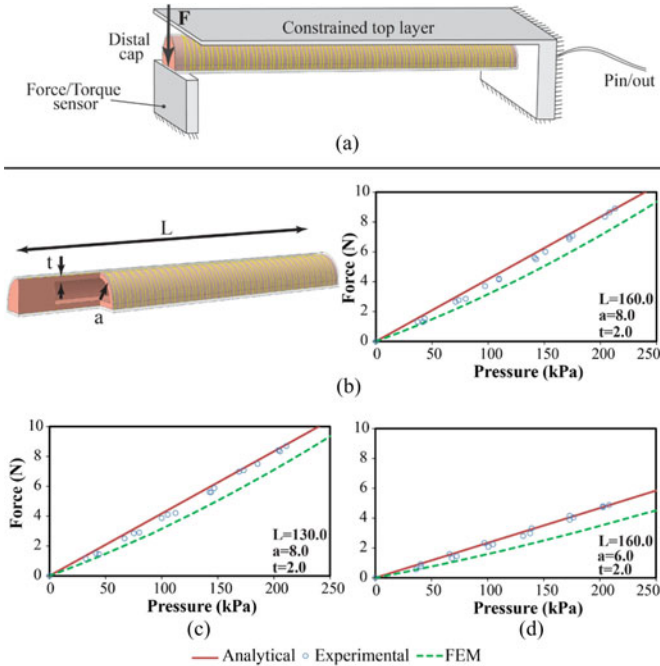
Fig. 11. Force responses measured at the distal tip of the actuators using the analytical model, FEM model, and experimental data (a) while the top layer of the actuator was constrained. (b) Force responses for an actuator with: 160.0-mm length, 8.0-mm radius, and 2.0-mm wall thickness. (c) Force responses for an actuator with: 130.0-mm length, 8.0-mm radius, and 2.0-mm wall thickness. (d) Force responses for an actuator with: 160.0-mm length, 6.0-mm radius, and 2.0-mm wall thickness.
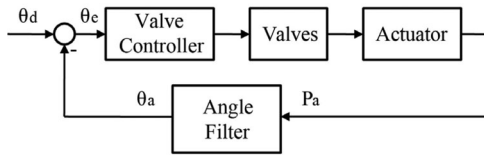

Fig. 12. Feedback control loop scheme with the analytical model embedded into the angle filter to calculate actuator bending angle from measured air pressure.

the state of the valves to remain unchanged until the input was changed adequately. This was expressed as

$$\theta_{\mathrm{DDZ}} = \pm \left(\frac{\theta_d}{k} + \theta_c \right) \qquad (22)$$

where $k = 50$ and $\theta_c = 0.07$ rad were parameters empirically selected to minimize oscillations. A larger θ_{DDZ} value made the valve controller more tolerant to signal noise, but also less agile to changes of θ_d and hence reduced its tracking performance, and *vice versa*.

The feedback control loop was tested in a step response experiment and a sinusoidal tracking experiment. For both signal forms, the time delay for the system to track the desired angle signal θ_d and the unintended switching of the valves were evaluated. In the step response test, as shown in Fig. 13(a), the actuator angle was able to follow the reference signal with an average convergence time of 91 ms and with an undesired valve switching of 0.85% of the total time. It is noted that the exhaust of the outlet valve was directly connected to the environment
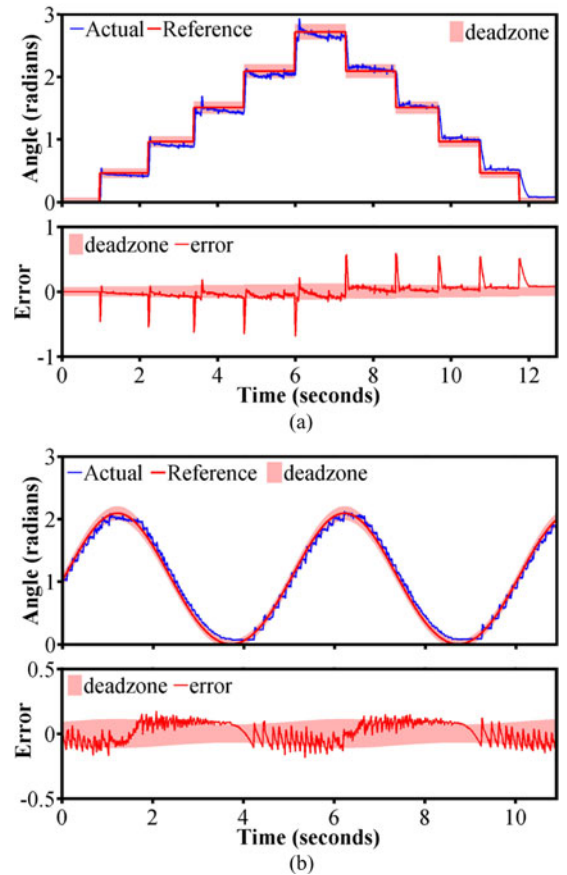

Fig. 13. Feedback control loop performance. (a) Step response of the actual signal (θ_a) and reference signal (θ_d), the angle error (θ_e) is shown with the deadzone. (b) Sinusoidal tracking performance with a reference signal (θ_d) of 0.2 Hz.

resulting in slower discharging speed (124 ms). In the sinusoidal experiment of Fig. 13(b), the actuator bending angle was successful in tracking a θ_d angle signal of 0.2 Hz with a tracking delay of 60 ms and an undesired valve switching of 0.5% of the total time.

VII. CONCLUSION

Soft fluidic actuators can generate complex 3-D outputs at a very low mechanical cost with simple control inputs. To date, the development of such actuators has largely been an empirical process. In order to enable the robotics research community to deterministically design new soft robotic systems and provide information on their performance prior to their manufacture, accurate and experimentally validated quasi-static computational (FEM) and analytical models were developed for a specific class of soft actuators, the soft fiber-reinforced bending actuator.

The FEM models provide the ability to simulate the function of the actuators and highlight local stress/strain concentrations such as where the fibers interacted with the elastomer. Alternatively, the simplified analytical approach provided a means of predicting actuator performance with explicit relationships between input pressure, actuator bending angle, and output force. The findings from the modeling work were also evaluated through experimental characterizations, which provided a better understanding of the individual parameters that affect the

TABLE II
COMPARISON BETWEEN DIFFERENT DESIGN PARAMETERS OF THE
SOFT FIBER-REINFORCED BENDING ACTUATOR

Increase in:	Required pressure at 360° (i)	Force generated at 0° and constant pressure (ii)
Radius	↓	↑
Length	↓	—
Wall Thickness	↑	n/a

↑: higher ↓: lower −: insignificant n/a: not available
(i) Required pressure to reach 360° bending angle. (ii) Force generation at the proximal cap for a constant pressure at 0° bending angle.

performance of these soft actuators (see qualitative parameter summary in Table II). Furthermore, a feedback control loop was created to demonstrate the ease of actuator controllability. In this case study, the analytical model for bending in free space was utilized to create an angle filter and estimate the bending angle of the soft actuator based only on the supplied air pressure. The valve controller of the feedback control loop was successful in tracking step and sinusoidal angle signals.

In the future, the dynamic behavior of the fiber-reinforced bending actuators will be investigated, and the methods for simulating, fabricating, and controlling other types of soft multimaterial fluidic actuators will be extended. Variations of the fiber winding pitch and fiber orientation will also be investigated to study the influence of these parameters on actuator performance, specifically, the types of motions that can be achieved with a single pressure control input.

APPENDIX

This analysis is to compare the bending torques (M_a) of internal air pressure against the distal cap of each actuator geometry. The first factor to consider is the cross-sectional area. For the same input pressure, the pressure-generated force on each actuator tip will be the same if each actuator has the same cross-sectional area. For this, if the area of each actuator is assumed to be a^2, the width and height of the RT shape and the radii of the HC and FC shape are hence

$$w_{\mathrm{RT}} = va, \ h_{\mathrm{RT}} = a/v, \ r_{\mathrm{HC}} = 0.80a, \ r_{\mathrm{FT}} = 0.56a$$

where v is the coefficient determining the height/width ratio of the rectangular shape.

Next, assuming the wall thicknesses of the actuators are $t = a/4$, the bending torques of each actuator shape around the bottom layer can be calculated as follows.

For RT shape:
The force generated by input pressure on each horizontal line of the actuator tip with distance α from the bottom layer is

$$f_{\mathrm{RT}} = vaP_{\mathrm{in}}d\alpha. \qquad (\mathrm{A1})$$

Hence, the torque becomes

$$M_a^{\mathrm{RT}} = \int_0^{\frac{a}{v}} f_{\mathrm{RT}} \left(\alpha + t\right) = \frac{1 + 0.5v}{2v}a^3 P_{\mathrm{in}} \qquad (\mathrm{A2})$$

For HC shape:
The force generated by input pressure on each horizontal line of the actuator tip with distance α from the bottom layer is

$$f_{\mathrm{HC}} = 2r_{\mathrm{HC}} \cos\theta P_{\mathrm{in}}d\alpha \qquad (\mathrm{A3})$$

where $\theta = a\sin\frac{\alpha}{r_{\mathrm{HC}}}$; hence, $\alpha = r_{\mathrm{HC}}\sin\theta$.
Therefore, the torque becomes

$$M_a^{\mathrm{HC}} = \int_0^{r_{\mathrm{HC}}} f_{\mathrm{HC}} \left(\alpha + \frac{a}{4}\right) = \frac{2}{3}P_{\mathrm{in}}r_{\mathrm{HC}}^3 + \frac{\pi P_{\mathrm{in}}r_{\mathrm{HC}}^2 a}{8}. \qquad (\mathrm{A4})$$

Substituting $r_{\mathrm{HC}} = 0.80a$,

$$M_a^{\mathrm{HC}} = \frac{2}{3}P_{\mathrm{in}}(0.8a)^3 + \frac{\pi P_{\mathrm{in}}(0.8a)^2 a}{8} = 0.59a^3 P_{\mathrm{in}}. \qquad (\mathrm{A5})$$

For FC shape:
The force generated by input pressure on each horizontal line of the actuator tip with distance α from the bottom layer is

$$f_{\mathrm{FC}} = 2r_{\mathrm{FC}} \sin\phi P_{\mathrm{in}}d\alpha \qquad (\mathrm{A6})$$

where $\phi = a\cos\frac{r_{\mathrm{FC}} - \alpha}{r_{\mathrm{FC}}}$; hence, $\alpha = r_{\mathrm{FC}}(1 - \cos\phi)$.
The torque then becomes

$$M_a^{\mathrm{FC}} = \int_0^{2r_{\mathrm{FC}}} f_{\mathrm{FC}} \left(\alpha + \frac{a}{4}\right)$$
$$= 2r_{\mathrm{FC}}P_{\mathrm{in}} \int_0^{2r_{\mathrm{FC}}} \sin\phi \left(\alpha + \frac{a}{4}\right) d\alpha. \qquad (\mathrm{A7})$$

Solving the above integration and substituting $r_{\mathrm{FT}} = 0.56a$ gives

$$M_a^{\mathrm{FC}} = \pi r_{\mathrm{FC}}^2 \left(r_{\mathrm{FC}} + \frac{a}{4}\right) P_{\mathrm{in}} = 0.80a^3 P_{\mathrm{in}}. \qquad (\mathrm{A8})$$

Equations (A2), (A5), and (A8) are the corresponding bending torques provided by the RT, HC, and FC shapes by supplied pressure on their tips, respectively. In particular, the coefficient v in (A2) is to be determined. In order to compare with the HC shape, v is chosen to give the RT shape the same M_a as the HC shape with the same input pressure P_{in}, such that

$$M_a^{\mathrm{RT}} = \frac{1 + 0.5v}{2v}a^3 P_{\mathrm{in}} = M_a^{\mathrm{HC}} = 0.59a^3 P_{\mathrm{in}}. \qquad (\mathrm{A9})$$

Therefore, the value of coefficient v can be calculated as

$$v = 1.46. \qquad (\mathrm{A10})$$

Hence, the RT shape with $v = 1.46$ has a cross-sectional width of $1.46a$ and a height of $a/1.46 = 0.68a$. Compared with the corresponding HC shape with a cross-sectional width of $2*0.8a = 1.6a$ and height of $0.8a$, the RT shape is notably narrower and shorter, while having both the same cross-sectional area and the same bending torque as the HC shape.

The pressure-induced bending torques in (A2), (A5), and (A8) alone do not fully describe the actuator characteristics during bending. Another important aspect is the internal material stretch moment occurring with the bending motion as a resistance. To quantify this, a model of the actuator internal stretch is required. Here, a similar approach is taken in comparison with

the modeling procedure presented in this paper, where the hyperelastic material behavior is modeled by the NH model, and only the axial direction principal stretch ratio λ_1 is considered (see Section III-B1). Therefore the different geometries of three actuator shapes could be considered separately, using the same variable notation as in Fig. 5 of Section III-B2.

For RT shape:

With actuator length L, bending angle θ, and overall actuator curve radius R (as shown in Fig. 5)

$$\lambda = \frac{d + R}{R} = \frac{\theta d}{L} + 1 \tag{A.11}$$

where d is the distance between the point where λ is defined to the actuator bottom. Therefore, the internal stretch moment combining the top, bottom, and side actuator walls becomes

$$
\begin{aligned}
M_\theta^{\mathrm{RT}} =\ & \int_{t+a/v}^{2t+a/v} va \cdot L \cdot d \cdot \mu \left(\lambda - \lambda^{-3} \right) \cdot dd \\
& + \int_0^t va \cdot L \cdot d \cdot \mu \left(\lambda - \lambda^{-3} \right) \cdot dd \\
& + 2 \int_0^{2t+a/v} t \cdot \mu \left(\lambda - \lambda^{-3} \right) \cdot L \cdot d \cdot dd.
\end{aligned}
\tag{A12}
$$

For HC shape, the result from (14) can be used (with $a = r_{\mathrm{HC}}$ and $b = t$):

$$
\begin{aligned}
M_\theta^{\mathrm{HC}} =\ & \int_0^t s_\beta \cdot 2 \left(r_{\mathrm{HC}} + t \right) L\beta d\beta \\
& + 2 \int_0^t \left(\int_0^{\frac{\pi}{2}} s_{\tau,\phi} \left((r_{\mathrm{HC}} + \tau)^2 \sin \phi \right. \right. \\
& \qquad \left. \left. + t(r_{\mathrm{HC}} + \tau) \right) L d\phi \right) d\tau.
\end{aligned}
\tag{A13}
$$

where s_β and $s_{\tau,\phi}$ are defined as in (15) and (18), respectively.

For FC shape:

The axial principal stretch λ is

$$
\begin{aligned}
\lambda &= \frac{t + R + r_{\mathrm{FC}} - (r_{\mathrm{FC}} + c) \cos \phi}{R} \\
&= \frac{t + r_{\mathrm{FC}} - (r_{\mathrm{FC}} + c) \cos \phi}{L} \theta + 1
\end{aligned}
\tag{A14}
$$

where c is the radial distance between the point where λ is defined to the actuator inner surface. Therefore, the internal stretch moment of the actuator wall becomes

$$
\begin{aligned}
M_\theta^{\mathrm{FC}} =\ & 2 \int_0^\pi \mu \left(\lambda - \lambda^{-3} \right) \left(\int_0^t \left((r_{\mathrm{FC}} + t)(r_{\mathrm{FC}} + c) \right. \right. \\
& \qquad \left. \left. - (r_{\mathrm{FC}} + c)^2 \cos \phi \right) L d\phi \right) dc.
\end{aligned}
\tag{A15}
$$

Numerically solving the integrals in (A12), (A13), and (A15), the internal stretch moments could be obtained for all three actuator shapes. Consequently, the bending resistance, as shown in Fig. 4(b), is defined as the ratio of the internal stretch moment over the supplied bending torque:

$$\text{Bending Resistance} = \frac{M_\theta}{M_a}. \tag{A16}$$

REFERENCES

[1] C. Majidi, "Soft Robotics: A perspective—Current trends and prospects for the future," *Soft Robot.*, vol. 1, pp. 5–11, 2013.

[2] F. Ilievski, A. D. Mazzeo, R. F. Shepherd, X. Chen, and G. M. Whitesides, "Soft robotics for chemists," *Angew. Chem.*, vol. 123, pp. 1930–1935, 2011.

[3] R. F. Shepherd, F. Ilievski, W. Choi, S. A. Morin, A. A. Stokes, A. D. Mazzeo, X. Chen, M. Wang, and G. M. Whitesides, "Multigait soft robot," *Proc. Nat. Acad. Sci.*, vol. 108, pp. 20400–20403, 2011.

[4] N. Correll, C. D. Onal, H. Liang, E. Schoenfeld, and D. Rus, "Soft autonomous materials—Using active elasticity and embedded distributed computation," presented at the Int. Symp. Exp. Robot., New Delhi, India, 2010.

[5] D. Trivedi, C. D. Rahn, W. M. Kier, and I. D. Walker, "Soft robotics: Biological inspiration, state of the art, and future research," *Appl. Bionics Biomech.*, vol. 5, pp. 99–117, 2008.

[6] S. Seok, C. D. Onal, R. Wood, D. Rus, and S. Kim, "Peristaltic locomotion with antagonistic actuators in soft robotics," in *Proc. IEEE Int. Conf. Robot. Autom.*, 2010, pp. 1228–1233.

[7] K. Suzumori, S. Endo, T. Kanda, N. Kato, and H. Suzuki, "A bending pneumatic rubber actuator realizing soft-bodied manta swimming robot," in *Proc. IEEE Int. Conf. Robot. Autom.*, 2007, pp. 4975–4980.

[8] L. Shi, S. Guo, M. Li, S. Mao, N. Xiao, B. Gao, Z. Song, and K. Asaka, "A novel soft biomimetic microrobot with two motion attitudes," *Sensors*, vol. 12, pp. 16732–16758, 2012.

[9] F. Carpi, S. Bauer, and D. De Rossi, "Stretching dielectric elastomer performance," *Science*, vol. 330, pp. 1759–1761, 2010.

[10] C. Keplinger, M. Kaltenbrunner, N. Arnold, and S. Bauer, "Röntgen's electrode-free elastomer actuators without electromechanical pull-in instability," *Proc. Nat. Acad. Sci.*, vol. 107, pp. 4505–4510, 2010.

[11] C. Laschi, M. Cianchetti, B. Mazzolai, L. Margheri, M. Follador, and P. Dario, "Soft robot arm inspired by the octopus," *Adv. Robot.*, vol. 26, pp. 709–727, 2012.

[12] H.-T. Lin, G. G. Leisk, and B. Trimmer, "GoQBot: A caterpillar-inspired soft-bodied rolling robot," *Bioinspir. Biomim.*, vol. 6, p. 026007, 2011.

[13] H. Lee, C. Xia, and N. X. Fang, "First jump of microgel; actuation speed enhancement by elastic instability," *Soft Matter*, vol. 6, pp. 4342–4345, 2010.

[14] M. Otake, Y. Kagami, M. Inaba, and H. Inoue, "Motion design of a starfish-shaped gel robot made of electro-active polymer gel," *Robot. Auton. Syst.*, vol. 40, pp. 185–191, 2002.

[15] E. Brown, N. Rodenberg, J. Amend, A. Mozeika, E. Steltz, M. R. Zakin, H. Lipson, and H. M. Jaeger, "Universal robotic gripper based on the jamming of granular material," *Proc. Nat. Acad. Sci.*, vol. 107, pp. 18809–18814, 2010.

[16] C. D. Onal and D. Rus, "A modular approach to soft robots," in *Proc. Biomed. Robot. Biomech.*, 2012, pp. 1038–1045.

[17] R. F. Shepherd, A. A. Stokes, J. Freake, J. Barber, P. W. Snyder, A. D. Mazzeo, L. Cademartiri, S. A. Morin, and G. M. Whitesides, "Using explosions to power a soft robot," *Angew. Chem.*, vol. 125, pp. 2964–2968, 2013.

[18] R. V. Martinez, J. L. Branch, C. R. Fish, L. Jin, R. F. Shepherd, R. Nunes, Z. Suo, and G. M. Whitesides, "Robotic tentacles with three dimensional mobility based on flexible elastomers," *Adv. Mater.*, vol. 25, pp. 205–212, 2013.

[19] C.-P. Chou and B. Hannaford, "Measurement and modeling of McKibben pneumatic artificial muscles," *IEEE Trans. Robot. Autom.*, vol. 12, no. 1, pp. 90–102, Feb. 1996.

[20] B.-S. Kang, C. S. Kothera, B. K. Woods, and N. M. Wereley, "Dynamic modeling of Mckibben pneumatic artificial muscles for antagonistic actuation," in *Proc. IEEE Int. Conf. Robot. Autom.*, 2009, pp. 182–187.

[21] J. Bishop-Moser, G. Krishnan, C. Kim, and S. Kota, "Design of soft robotic actuators using fluid-filled fiber-reinforced elastomeric enclosures in parallel combinations," in *Proc. IEEE/RSJ Int. Conf. Intell. Robot. Syst.*, 2012, pp. 4264–4269.

[22] E. T. Roche, R. Wohlfarth, J. T. B. Overvelde, N. V. Vasilyev, F. A. Pigula, D. J. Mooney, K. Bertoldi, and C. J. Walsh, "A bioinspired soft actuated material," *Adv. Mater.*, vol. 26, no. 8, pp. 1200–1206, 2014.

[23] R. V. Martinez, C. R. Fish, X. Chen, and G. M. Whitesides, "Elastomeric origami: Programmable paper elastomer composites as pneumatic actuators," *Adv. Func. Mater.*, vol. 22, pp. 1376–1384, 2012.

[24] Y. Sun, Y. S. Song, and J. Paik, "Characterization of silicone rubber based soft pneumatic actuator," in *Proc. IEEE/RSJ Int. Conf. Intell. Robot. Syst.*, 2013, pp. 4446–4453.

[25] B. Tondu and P. Lopez, "Modeling and control of McKibben artificial muscle robot actuators," *IEEE Control Syst. Mag.*, vol. 20, no. 2, pp. 15–38, Apr. 2000.

[26] J. Hiller and H. Lipson, "Automatic design and manufacture of soft robots," *IEEE Trans. Robot.*, vol. 28, no. 2, pp. 457–466, Apr. 2012.

[27] D. Trivedi, C. D., Rahn, W. M., Kier, and I. D., Walker, "Soft robotics: Biological inspiration, state of the art, and future research," *Appl. Bionics Biomech.*, vol. 5, no. 3, pp. 99–117, 2008.

[28] S. Kim, C. Laschi, and B. Trimmer, "Soft robotics: A bioinspired evolution in robotics," *Trends Biotechnol.*, vol. 31, no. 5, pp. 287–294, 2013.

[29] R. Deimel and O. Brock, "A compliant hand based on a novel pneumatic actuator," in *Proc. IEEE Int. Conf. Robot. Autom.*, Karlsruhe, Germany, May 2013, pp. 2047–2053.

[30] R. Deimel and O. Brock, "A novel type of compliant, underactuated robotic hand for dexterous grasping," *Robot.: Sci. Syst.*, pp. 1687–1692, 2014.

[31] K. C. Galloway, P. Polygerinos, C. J. Walsh, and R. J. Wood, "Mechanically programmable bend radius for fiber-reinforced soft actuators," in *Proc. IEEE Int. Conf. Adv. Robot.*, Montevideo, Uruguay, Nov. 2013, pp. 1–6.

[32] F. Daerden and D. Lefeber, "Pneumatic artificial muscles: Actuators for robotics and automation," *Eur. J. Mech. Environ. Eng.*, vol. 47, pp. 11–21, 2002.

[33] R. W. Ogden, *Non-Linear Elastic Deformations*. Mineola, NY, USA: Courier Dover Publications, 1997.

[34] A. M. Faudzi, M. R. M. Razif, I. N. A. M. Nordin, K. Suzumori, S. Wakimoto, and D. Hirooka, "Development of bending soft actuator with different braided angles," in *Proc. IEEE/ASME Int. Conf. Adv. Intel. Mech.*, 2012, pp. 1093–1098.

[35] A. Manuello Bertetto and M. Ruggiu, "Characterization and modeling of air muscles," *Mech. Res. Commun.*, vol. 31, pp. 185–194, 2004.

[36] P. Polygerinos, S. Lyne, Z. Wang, L. Fernando, B. M. Nicolini, G. M. Whitesides, and C. J. Walsh, "Towards a Soft Pneumatic Glove for Hand Rehabilitation." in *Proc. IEEE/RSJ Int. Conf. Intell. Robot. Syst.*, Tokyo, Japan, Nov. 2013, pp. 1512–1517.

[37] O. Yeoh, "Some forms of the strain energy function for rubber," *Rubber Chem. Technol.*, vol. 66, pp. 754–771, 1993.

[38] (2015, Jan.). [Online]. Available: http://softroboticstoolkit.com/book/fr-fabrication

Panagiotis Polygerinos (M'11) received the B.Eng. degree in mechanical engineering from Technological Educational Institute of Crete, Heraklion, Greece, in 2006, and the M.Sc. (with distinction) degree in mechatronics and the Ph.D. degree in mechanical engineering/medical robotics from King's College London, London, U.K., in 2007 and 2011, respectively.

He is a Technology Development Fellow with Wyss Institute and the School of Engineering and Applied Sciences, Harvard University, Cambridge, MA, USA, where he specializes in soft robotic systems that find application in wearables, medical, and rehabilitation areas.

Zheng Wang (M'10) received the B.Sc. degree (with merit) from Tsinghua University, Beijing, China; the M.Sc. degree (with distinction) from Imperial College London, London, U.K.; and the Ph.D. degree (with merit) from Technische Universität München, München, Germany.

He was a Postdoctoral Research Fellow with Nanyang Technological University, Singapore, between 2010 and 2013 and a Postdoctoral Fellow with the School of Engineering and Applied Sciences and Wyss Institute of Bioinspired Engineering, Harvard University, between 2013 and 2014. Since July 2014, he has been an Assistant Professor with the Department of Mechanical Engineering, University of Hong Kong, Hong Kong. His research interest include haptics human–robot interaction, teleoperation, cable-driven mechanisms, and soft robotics.

Johannes T. B. Overvelde received the B.Sc. and M.Sc. degrees (both with distinction) in mechanical engineering from Delft University of Technology, Delft, The Netherlands, in 2012. He is currently working toward the Ph.D. degree in applied mathematics with Katia Bertoldi's Group, School of Engineering and Applied Sciences, Harvard University, Cambridge, MA, USA.

His research interests include the field of structural optimization and computational mechanics.

Kevin C. Galloway received the B.S.E. and Ph.D. degrees in mechanical engineering from University of Pennsylvania, Philadelphia, PA, USA.

He is a Research Engineer with the Advanced Technology Team, Wyss Institute, Harvard University, Cambridge, MA, USA. His research interests are in applying knowledge of materials and prototyping techniques toward the development of bioinspired robots and medical devices.

Robert J. Wood received the Master's and Ph.D. degrees in electrical engineering from University of California, Berkeley, CA, USA, in 2001 and 2004, respectively.

He is an Associate Professor with the School of Engineering and Applied Sciences and the Wyss Institute for Biologically Inspired Engineering, Harvard University, Cambridge, MA, USA. His research interests include the areas of microrobotics and bioinspired robotics.

Katia Bertoldi received the Master's degrees from University of Trento, Trento, Italy, in 2002, and from Chalmers University of Technology, Göteborg, Sweden, in 2003, majoring in structural engineering mechanics, and the Ph.D. degree in mechanics of materials and structures from University of Trento in 2006.

She then joined the group of Mary Boyce, Massachusetts Institute of Technology, Cambridge, MA, USA, as a Postdoctoral Researcher. In 2008, she moved to University of Twente, Twente, The Netherlands, where she was an Assistant Professor with the faculty of Engineering Technology. In January 2010, she joined the School of Engineering and Applied Sciences, Harvard University, Cambridge, as an Associate Professor of applied mechanics and established a group studying the mechanics of materials and structures.

Conor J. Walsh (M'12) received the B.A.I. and B.A. degrees in mechanical and manufacturing engineering from Trinity College Dublin, Dublin, Ireland, in 2003, and the M.S. and Ph.D. degrees in mechanical engineering from Massachusetts Institute of Technology, Cambridge, MA, USA, in 2006 and 2010, respectively, with a minor in entrepreneurship through the Sloan School of Management and also a Certificate in Medical Science through the Harvard–MIT Division of Health Sciences and Technology.

He is an Assistant Professor with the Harvard School of Engineering and Applied Sciences and a Core Faculty Member with Wyss Institute for Biologically Inspired Engineering, Harvard University, Cambridge. He is the Founder of the Harvard Biodesign Laboratory, which brings together researchers from the engineering, industrial design, apparel, clinical, and business communities to develop new technologies and translate them to industrial partners. His research focuses on new approaches to the design, manufacture, and control of soft wearable robotic devices for augmenting and restoring human performance, and evaluating them through biomechanical and physiological studies.